applied sciences

MDPI

Article

Study on the Vibration Effects of Rock Slopes Under Blasting Loads

Junkai Chen [1,*], Youliang Chen [1,2], Suran Wang [1], Xiaojun Zhang [3] and Wenxue Gao [3]

[1] Department of Civil Engineering, School of Environment and Architecture, University of Shanghai for Science and Technology, Shanghai 200093, China; chenyouliang2001@163.com (Y.C.); wangsuran@usst.edu.cn (S.W.)
[2] Department of Engineering Geology and Hydrogeology, RWTH Aachen University, 52064 Aachen, Germany
[3] College of Architecture and Civil Engineering, Beijing University of Technology, Beijing 100124, China; zhangxj@bjut.edu.cn (X.Z.); wxgao@bjut.edu.cn (W.G.)
* Correspondence: 251640211@st.usst.edu.cn

Abstract

Engineering blasting is indispensable in national economic development; however, blast-induced vibration, recognized as a primary detrimental effect, necessitates rigorous investigation. This study delves into the dynamic response characteristics of rock slopes subjected to blasting loads. Leveraging a practical engineering context, field vibration monitoring was conducted during bench blasting excavation of a rock slope. Subsequently, a numerical model was developed to simulate the dynamic response of the rock slope, enabling a systematic analysis of the variations and distribution patterns of peak particle velocity (PPV), stress fields, and displacement fields within the rock mass. Key findings indicate that at the slope crest, the PPV of particles consistently attenuates with increasing distance from the blast center, with the rate of attenuation progressively diminishing as this distance extends. On the slope surface, an observable elevation amplification effect manifests on adjacent benches. Furthermore, a pronounced "whip-tail effect" is evident at the outer edge of individual benches, which gradually mitigates with ascending elevation. Post-blasting observations confirm the stability of the slope rock mass, characterized by distinct contours and uniform rock fragmentation, thereby offering valuable insights for analogous engineering endeavors.

Keywords: blasting vibration; deep hole blasting; vibration effect; vibration monitoring; whip-tail effect

1. Introduction

The relentless expansion of highway and railway networks into western mountainous regions and geologically intricate environments presents formidable challenges for subgrade engineering, particularly concerning excavation complexity and stringent geological conditions. Deep-hole bench blasting technology has garnered widespread application in cutting excavation and high slope trimming projects, primarily owing to its superior operational efficiency, robust adaptability, and controllable cost implications [1–3]. The intricate mechanisms governing the influence of blast vibration on slope stability are characterized by pronounced multi-scale coupling and inherent nonlinear uncertainties. On one hand, the propagation of blast seismic waves through geomaterials is intricately governed by geological structures, topographic features, and rock mass discontinuities, leading to complex attenuation laws and diverse spectral evolution characteristics [4–6]. On the other

Check for updates

Received: 30 July 2026
Revised: 4 September 2026
Accepted: 9 September 2026
Published: 11 September 2026

Copyright: © 2026 by the authors. Licensee MDPI, Basel, Switzerland. This article is an open access article distributed under the terms and conditions of the Creative Commons Attribution (CC BY) license.

hand, the dynamic response of slopes under transient loads involves a confluence of multi-physical field coupling processes, including stress wave reflection and diffraction, elevation amplification phenomena, and cumulative damage within jointed rock masses, which collectively render accurate vibration prediction and comprehensive safety assessment particularly challenging [7–9].

Recent advancements in precision delay blasting technologies, notably electronic detonators, have propelled the optimization of hole network parameters and millisecond-delay networks as a focal point for achieving active vibration control [10–13]. Consequently, it is imperative to integrate the waveform characteristics of single-hole blasting with field experimental data to ascertain optimal delay strategies. Precise control over inter-hole and inter-row delays is crucial for the active regulation of blast vibration [14–16]. Both empirical field monitoring and sophisticated numerical analyses consistently demonstrate a distinct "whip-tail effect" in bench slopes, wherein instantaneous accelerations at the slope crest significantly surpass those at the slope toe. This phenomenon is exacerbated by the geometric configuration of free surfaces, which induces wave reflection superposition, thereby intensifying the dynamic response of the upper rock mass. Practical engineering experience underscores that bench height is a pivotal determinant of the permissible vibration velocity. Specifically, reduced bench heights can lead to an elevated PPV ratio, thereby necessitating careful consideration of the coupled effects of slope geometry and bench height when establishing safety thresholds [17–21].

This paper undertakes a comprehensive and systematic investigation into the vibration effects on a cutting slope rock mass subjected to blasting loads, drawing upon a specific highway-cutting, slope-blasting project in China as its foundational context. The research methodology integrates theoretical analysis, meticulous blast vibration monitoring, and advanced finite element numerical simulation. The findings of this study are anticipated to furnish scientifically robust methodologies and foundational insights for addressing the dynamic stability concerns prevalent in high and steep rock slopes, thereby possessing substantial theoretical guidance and promising engineering application prospects [22,23]. The novelty of this study lies in three aspects: (1) integration of field vibration monitoring with a high-resolution 3D numerical model for a multi-bench highway cutting slope; (2) systematic quantification of the whip-tail effect distribution across multiple bench levels, which has rarely been examined in previous studies; (3) provision of quantitative PPV attenuation curves validated by field data for reference in similar projects.

2. Bench Blasting and Vibration Monitoring

2.1. Project Overview

The subject highway, situated in Beijing, China, boasts a designed total length of approximately 3.67 km. It is classified as a secondary highway, engineered for a design speed of 60 km/h. The road right-of-way spans 30 m, with a planned cross-section featuring a subgrade width of 10 m and a pavement width of 8.5 m.

The highway alignment traverses a river valley, extending from northwest to southeast, characterized by a gradual descent in elevation. The mountain peaks flanking the route exhibit a largely uniform geomorphology, predominantly presenting as circular or mound-shaped formations. Isolated sections, however, display abrupt cliffs resulting from rock layer discontinuities. The terrain preceding the villages comprises a series of parallel alluvial fan formations and isolated residual hills ranging from 50 to 100 m in elevation, with relatively subtle and undulating topographical variations.

The subgrade blasting section is situated within a 50–200 m radius of existing tunnels, bridge construction sites, and residential villages. The environmental context surrounding the blasting site is visually represented in Figure 1.



Figure 1. Surrounding environment of blasting site.

2.2. Design of Bench Blasting Parameters

The majority of the highway alignment comprises semi-excavated cuttings, with the blasting section requiring a maximum excavation height of approximately 30 m. The designed slope ratio for the cutting is 1:0.3, and the slope configuration incorporates a stepped bench arrangement. Based on the design specifications for the excavated section, the inherent engineering properties, and the estimated volume of rock blasting, a deep-hole blasting scheme was selected. To mitigate the impact of blasting on the stability of the cutting slope, buffer blasting techniques were implemented in proximity to the designed slope surface. This involved meticulous control over hole network parameters and individual hole charge weights to minimize blast-induced vibrations affecting the rock mass stability. Down-the-hole drilling was employed during the blasting operations, utilizing a hole diameter D = 90 mm. The drilling depth was precisely determined by considering both the excavation height and the required over-drilling depth. For the semi-excavated cutting section detailed in this study, blasting was executed in three distinct stages, progressing from top to bottom, with inclined boreholes. Adhering to conventional engineering practices for calculating burden W, hole spacing a, and row spacing b, the design parameters were established as follows: W = 2.5~3.0 m, a = 2.5~3.0 m, b = 2.0~2.5 m. The drilling inclination angle was set at 75°. The above parameters were determined according to the Chinese blasting safety standard (GB 6722-2014) [24] and engineering experience from similar highway cutting projects in Beijing. Concurrently, the stemming length was determined within the range of (0.7~1.0)W, with an emphasis on enhancing stemming quality. For buffer holes, their spacing was set at 0.7 times that of the main production holes. A representative cross-section illustrating the blasthole arrangement for the subgrade is presented in Figure 2.

The charge weight for individual holes was computed using a multi-boundary charge formula. In the context of multi-row blasting, and commencing from the second row, an increase of 10% to 15% in the charge weight was applied to each hole, accounting for the confinement effect exerted by the rock mass. The standard specific charge for throw blasting, denoted as K, was adopted as 1.3~1.4 kg/m^3. Given a natural ground slope α ranging from 60° to 75°, the calculated single-hole charge weights for main holes at varying depths are tabulated in Table 1. The specific charge K = 1.3–1.4 kg/m^3 was adopted from standard practice for throw blasting in medium-hard limestone [24]. The drilling inclination of 75° was set to match the designed slope ratio of 1:0.3. Notably, the charge

weight for buffer holes was approximately half of the corresponding single-hole charge listed in the table.

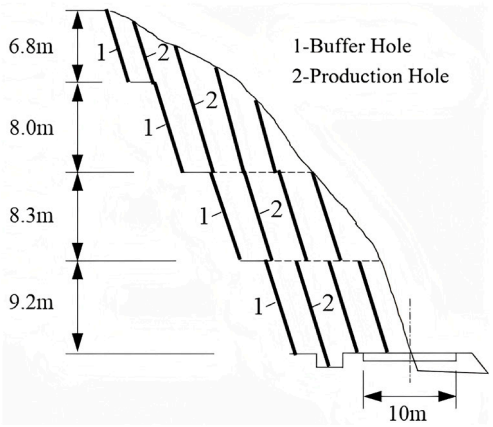


Figure 2. Cross section of the blasthole.

Table 1. Deep hole blasting parameter table.

Hole Depth L (m)	Hole Spacing a (m)	Row Spacing b (m)	KF [E, α] (kg/m^3)	Q (kg)	L_2 (m)
6	2.5	2.0	0.405	15.19	2.0
8	2.5	2.0	0.405	20.25	2.0
10	2.8	2.2	0.417	32.69	2.5
12	2.8	2.2	0.417	39.23	2.5
14	3.0	2.5	0.429	54.05	3.0
16	3.0	2.5	0.429	61.78	3.0

2.3. Determination of Millisecond-Delay Time

The precise determination of appropriate delay intervals is paramount for achieving controlled blasting outcomes. Equation (1) was employed to calculate the inter-hole delay time.

This is the first equation.

$$\Delta t_1 = (20 \sim 40)W/f \quad (1)$$

In Equation (1), Δt_1 represents the inter-hole delay interval time in milliseconds (ms); W denotes the burden in meters (m); and f signifies the rock tenacity coefficient. For this project, W = 2.8 m (average burden) and f = 8 (rock tenacity coefficient for limestone) were substituted, yielding Δt_1 = 25 ms.

Adhering to the principle that delayed blasting enhances the creation of free faces, the blast crater generated by the initial hole detonation establishes a new free face for subsequent borehole blasting. Consequently, the inter-row delay time should be at least one to two inter-hole delay intervals greater than that of the preceding row of holes in the same column. The design of the inter-row delay time was guided by Equation (2).

$$\Delta t_2 = [k\Delta t_1 + (k+1)\Delta t_1]/2 \quad (2)$$

In Equation (2), Δt_2 denotes the inter-row delay interval time in milliseconds (ms); k represents the number of holes in the subsequent row that are initiated later than the corresponding holes in the preceding row; and Δt_1 is the inter-hole delay interval time. With k = 2 and Δt_1 = 25 ms, the inter-row delay was calculated as $\Delta t_2 = (2 \times 25 + 3 \times 25)/2$ = 75 ms.

Based on calculations derived from Equation (1), the inter-hole delay time was determined to be 25 ms. Subsequently, utilizing Equation (2), the inter-row delay time was set at 75 ms. Considering the inherent rock mass characteristics of the subgrade blasting excavation section, and comprehensively evaluating factors such as prevailing topographic conditions, anticipated blast seismic intensity, desired rock fragmentation efficacy, and the reliability of the blasting network, the final blasting scheme incorporated an in-hole delay of MS12 (550 ms), an inter-hole delay of MS2 (25 ms), and an inter-row delay of MS4 (75 ms). The complete blasting network configuration is depicted in Figure 3.

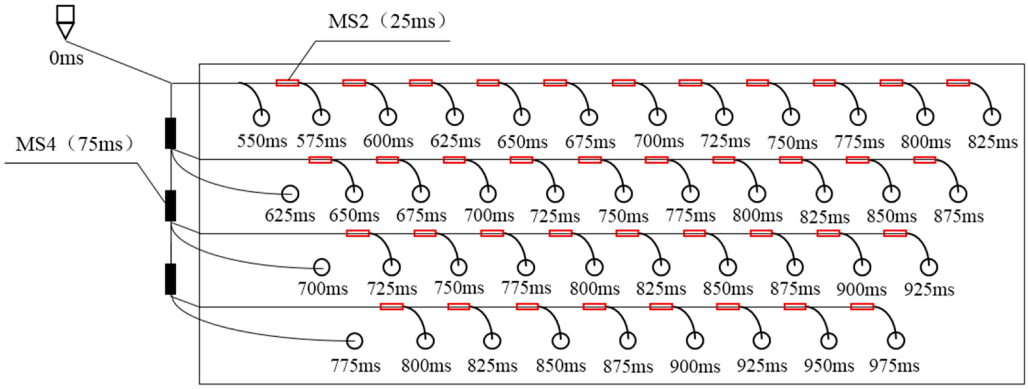


Figure 3. Blasting network connection diagram.

2.4. Blast Vibration Monitoring

To ensure the integrity and reliability of the acquired test data, the ground surface at each monitoring point was meticulously prepared prior to instrument deployment. Sensors were securely affixed to the ground using plaster, ensuring stable contact. Vibration response tests were initiated only after the plaster had fully cured. In accordance with the experimental design and monitoring objectives, a total of five monitoring points (designated 1# to 5#) were strategically positioned at the slope crest and within the surrounding area. These points were arranged at the slope crest with a horizontal spacing of 5 m, with point 1# situated approximately 5 m from the outer edge of the slope crest. The precise spatial arrangement of these monitoring points is illustrated in Figure 4. The five monitoring points were arranged in a single row along the slope crest with a horizontal spacing of 5 m. Point 1# was located approximately 5 m from the outer edge of the slope crest (see Figure 4).

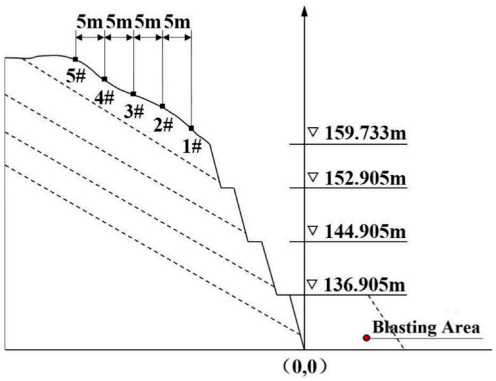


Figure 4. Location of monitoring points. 1# to 5# denote the five monitoring points arranged along the slope crest.

The vibration response testing system employed on-site, depicted in Figure 5, possessed a frequency response range of 0~10 kHz and a sampling frequency adjustable

between 1~50 kHz. The raw data collected from the blast vibration tests are systematically summarized in Table 2. The vibration testing system (model TC-4850, Chengdu Zhongke Measurement and Control Co., Ltd., Chengdu City, China) had a frequency response range of 0~10 kHz and a sampling frequency of 1~50 kHz. Data were processed using MATLAB R2021a with Fast Fourier Transform to extract PPV values.



Figure 5. Photographs of monitoring points.

Table 2. Summary table of vibration monitoring data.

Point Number	Blast Center Distance (m)		Peak Particle Velocity (m/s)		
	Horizontal Component	Vertical Component	Horizontal Radial (X)	Horizontal Tangential (Y)	Vertical (Z)
1#	41.23	36.49	0.04267	0.03188	0.05186
2#	46.23	39.52	0.03174	0.02416	0.04382
3#	51.23	41.98	0.01548	0.01528	0.02074
4#	56.23	43.05	0.01098	0.01032	0.01496
5#	61.23	47.16	0.00796	0.00481	0.01437

3. Dynamic Response of Slope Rock Mass Under Bench Blasting

3.1. Calculation Model

Within the numerical model, the rock mass material was characterized by an elasto-plastic constitutive relationship, with the Mohr–Coulomb criterion serving as the adopted yield criterion. The Mohr–Coulomb continuum model was adopted as a first-order engineering approximation suitable for the scale of this analysis. Equivalent blasting loads were applied for the computational analysis. Based on comprehensive geological survey reports and results from indoor geotechnical laboratory tests, the physico-mechanical parameters assigned to the rock mass are presented in Table 3. The parameters were determined from laboratory tests on core samples and the geological survey report. While the rock mass is not strictly homogeneous, an equivalent continuum model was adopted as a reasonable engineering-scale simplification [5].

Table 3. Physico-mechanical parameters of the rock mass.

Rock Mass	E_r (GPa)	E_{oed} (GPa)	G_r (GPa)	ρ (kg/m^3)	v	c (MPa)	φ (°)	R_m (MPa)
Cambrian Limestone	19.64	26.438	7.554	2710	0.24	2.45	51	1.1

In Table 3, E_r denotes the elastic modulus; E_{oed} represents the oedometric modulus; G_r signifies the shear modulus; ρ is the density; v is Poisson's ratio; c is the cohesion; φ is the friction angle; and R_m is the tensile strength.

The mesh element sizes were selected as follows: 0.03 m near the boreholes, 0.2–0.5 m along the slope surface, and 1–2 m at the model boundaries. The three-dimensional finite element model of the slope is graphically depicted in Figure 6.

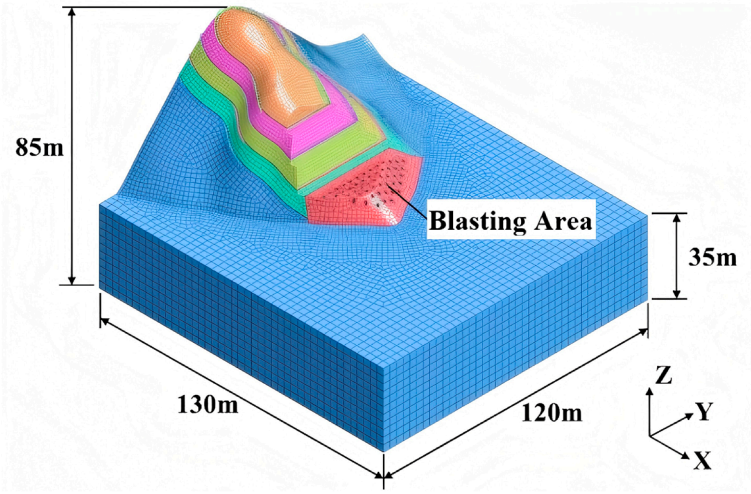


Figure 6. Numerical model of the slope.

3.2. Validation of the Numerical Model

To validate the numerical model, the peak particle velocities at monitoring points corresponding to the field measurement locations were extracted and compared with the vibration monitoring data listed in Table 2. The positions of the five monitoring points within the numerical model are illustrated in Figure 7.

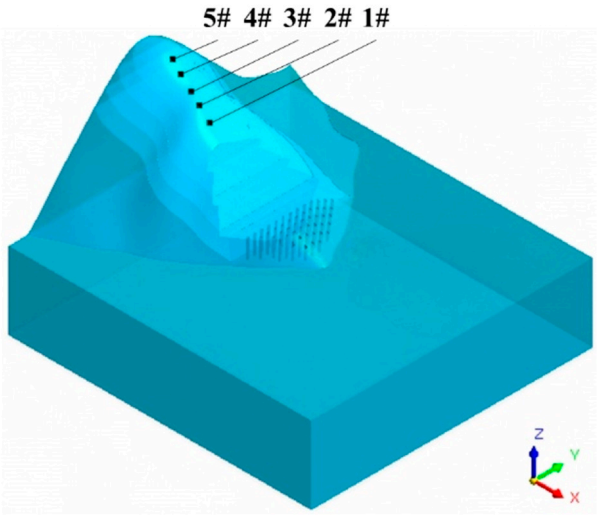


Figure 7. Location of measurement points. 1# to 5# denote the five monitoring points arranged along the slope crest.

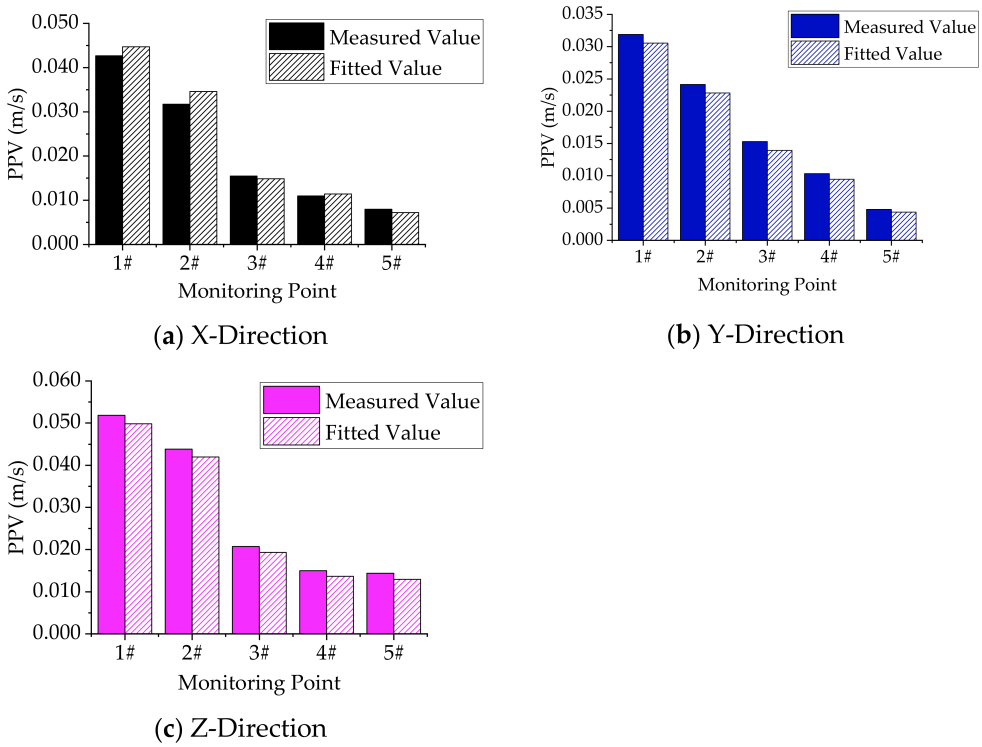
The peak particle velocities (PPV) obtained from the numerical simulation were extracted and compared with the field monitoring data at the corresponding measuring points (Table 2, Section 2.4). The comparison results are summarized in Table 4.

Table 4. Statistical comparison table.

Direction	Monitoring Point ID	Measured Value (m/s)	Fitted Value (m/s)	Relative Error (%)
X-Direction	1#	0.04267	0.04473	4.828
	2#	0.03174	0.03458	8.948
	3#	0.01548	0.01487	3.941
	4#	0.01098	0.01139	3.734
	5#	0.00796	0.00721	9.422
Y-Direction	1#	0.03188	0.03053	4.235
	2#	0.02416	0.02284	5.464
	3#	0.01528	0.01392	8.901
	4#	0.01032	0.00945	8.430
	5#	0.00481	0.00437	9.148
Z-Direction	1#	0.05186	0.04985	3.876
	2#	0.04382	0.04196	4.245
	3#	0.02074	0.01932	6.847
	4#	0.01496	0.01363	8.890
	5#	0.01437	0.01297	9.743

Relative Error = |(Fitted Value – Measured Value)/Measured Value| × 100%.

For a more intuitive comparison, the simulated and measured peak particle velocities at the corresponding monitoring points are presented as a bar chart in Figure 8.



(**a**) X-Direction

(**b**) Y-Direction

(**c**) Z-Direction

Figure 8. Comparison between measured and fitted values.

As shown in Table 4 and Figure 8, the numerical simulation results are in good agreement with the measured data, with all relative errors within 10% [25], indicating that the numerical model exhibits satisfactory reliability.

3.3. Blasting Load Application Method

This study employs a triangular distributed load as its fundamental basis, incorporating the load arrival time to account for the delay times of explosives in individual boreholes.

This approach facilitates the simulation of the superposition of blast-induced stress waves. The time history of a single load was meticulously derived from established detonation wave theory and blast cavity expansion theory.

The triangular distributed load is widely adopted as an engineering simplification for blast analysis. Its limitations include the inability to capture detailed detonation wave interactions and delay errors; more sophisticated models (ALE or SPH) could be used in future work.

For a triangular load profile, it is essential to precisely determine the peak blasting intensity, the pressure rise time, and the duration of the positive pressure phase. The pressure at the detonation wave front during explosive detonation is given by [26]:

$$P_D = \frac{\rho_0 D^2}{K+1} \tag{3}$$

In Equation (3), P_D represents the Chapman-Jouguet (C-J) pressure of the explosive;ρ_0 is the explosive density; D is the detonation velocity of the explosive; and K is the isentropic exponent of the explosive.

In the scenario of coupled charging, the peak intensity of the blasting load is approximately half of the C-J pressure, expressed as:

$$P_0 = \frac{P_D}{2} = \frac{\rho_0 D^2}{2(K+1)} \tag{4}$$

For uncoupled charging, particularly when the uncoupling coefficient is small, the peak pressure of the blasting load is calculated using the following equation:

$$P_0 = \frac{P_D}{2} = \frac{\rho_0 D^2}{2(K+1)} \left(\frac{d_c}{d}\right)^{2K} \tag{5}$$

In Equation (5), d_c denotes the charge diameter; and d represents the borehole diameter.

The rise time tr of the blasting load is computed using Equation (6) [27]:

$$t_r = 12\sqrt{r^{2-\mu}} Q^{0.05} / E_V \tag{6}$$

The duration of the positive pressure phase t_s of the blasting load is determined by Equation (7) [27]:

$$t_s = 84\sqrt[3]{r^{2-\mu}} Q^{0.2} / E_V \tag{7}$$

In Equation (6): E_V signifies the bulk modulus of the rock mass; r is the scaled distance; μ represents Poisson's ratio of the rock mass; and Q is the charge weight.

In millisecond-delay blasting, the resultant blast vibration is a temporal superposition of the individual vibration effects from each borehole. Assuming that the waveform generated by millisecond-delay blasting can be accurately synthesized by superimposing the waveforms from single-stage blasting events, the composite vibration waveform for millisecond-delay blasting can be mathematically expressed as [28]:

$$V = V_S \sum_{i=1}^{n} [a_i \cdot \delta_i(t - t_i)] \tag{8}$$

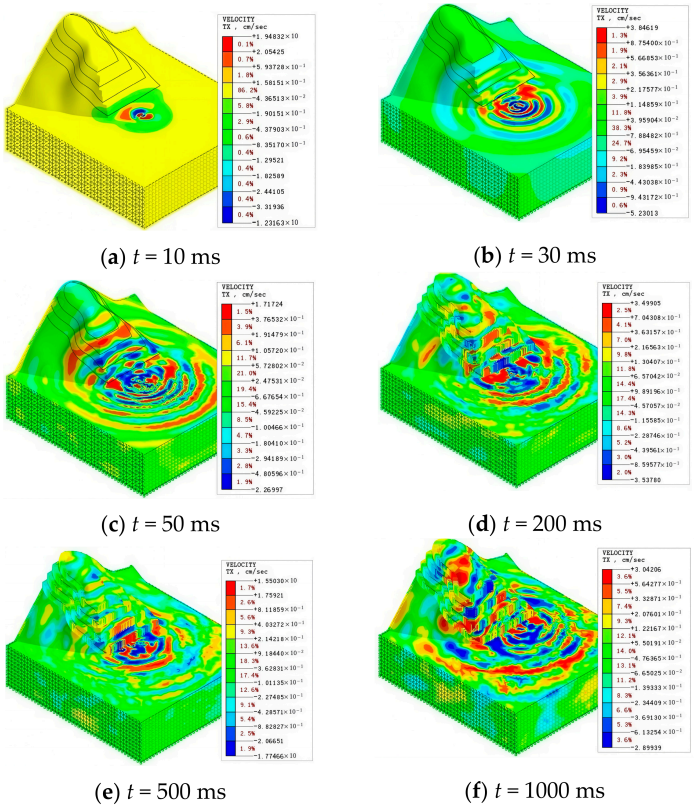
In Equation (8): V_S denotes the single-stage blasting waveform; n represents the total number of millisecond-delay blasting stages, where $n \in \{1, 2, 3, \ldots\}$; i is the sequential index of the millisecond-delay blasting stage; δ_i signifies the blast vibration impulse function corresponding to the i-th stage; t_i is the initiation time of the i-th stage, which corresponds to the delay time; and a_i is the scaling coefficient representing the ratio of the explosive

charge Q_i for the i-th stage to the reference charge Q_0 used in calculating the single-stage blasting.

For the specific engineering project examined in this paper, the explosive type, charge weight, and associated parameters were uniform across all boreholes, thus $a_i = 1$. The applied equivalent distributed load was linearly superimposed based on the inter-hole and inter-row delays. Consistent with the established blasting design scheme, each single-hole vibration waveform was considered to be mutually independent.

3.4. Analysis of Vibration Velocity Contour Maps of Slope Rock Mass

Figures 9–11 present the spatial distribution of blast vibration velocity contour maps within the slope rock mass, depicted at various time instances and across different directions. The visualizations reveal that under bench blasting conditions, the propagation characteristics of blast stress waves closely resemble those generated by concentrated charges, exhibiting an outward radial spread from the blasting zone with a concomitant gradual attenuation. Notably, the vibration velocity of rock mass particles in the immediate vicinity of the boreholes is considerably elevated. At an elapsed time of 10 ms, the instantaneous peak vibration velocities in the three principal directions attain magnitudes of 0.1948 m/s, 0.2149 m/s, and 0.1519 m/s, respectively. As time progresses, the blast energy progressively dissipates due to the inherent damping properties of the medium, leading to a rapid decay in peak vibration velocity. By 50 ms, the instantaneous peak vibration velocities in the three directions have diminished to 0.01717 m/s, 0.01884 m/s, and 0.02849 m/s, respectively. Subsequently, the explosives in the remaining boreholes are sequentially initiated, resulting in an increase in vibration velocity attributable to the superposition and interference of stress waves. At 1000 ms, the maximum vibration velocities observed among all rock mass particles in the three directions are 0.0304 m/s, 0.0277 m/s, and 0.0357 m/s, respectively.

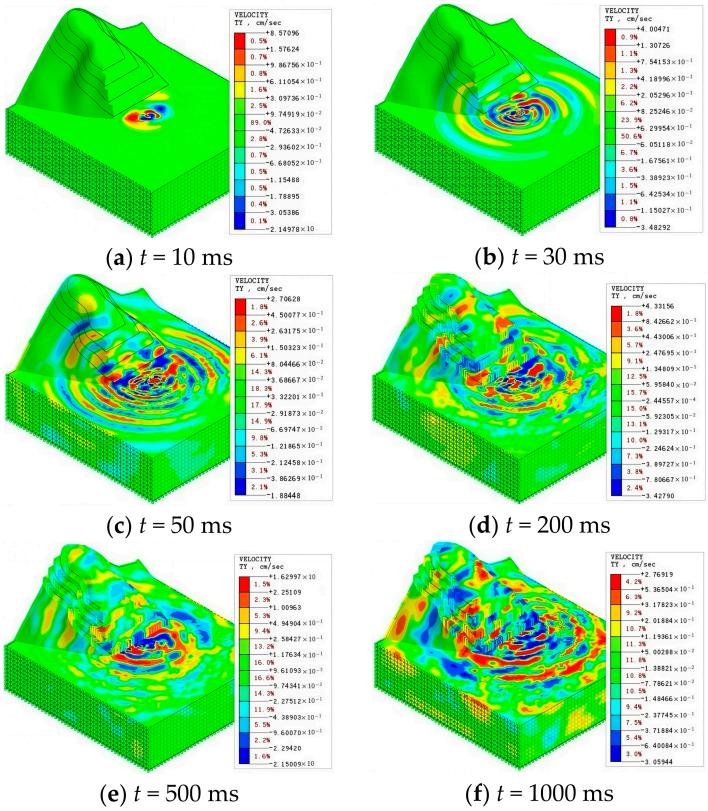


(**a**) t = 10 ms (**b**) t = 30 ms

(**c**) t = 50 ms (**d**) t = 200 ms

(**e**) t = 500 ms (**f**) t = 1000 ms

Figure 9. Vibration velocity contour of the rock mass in the X-direction.

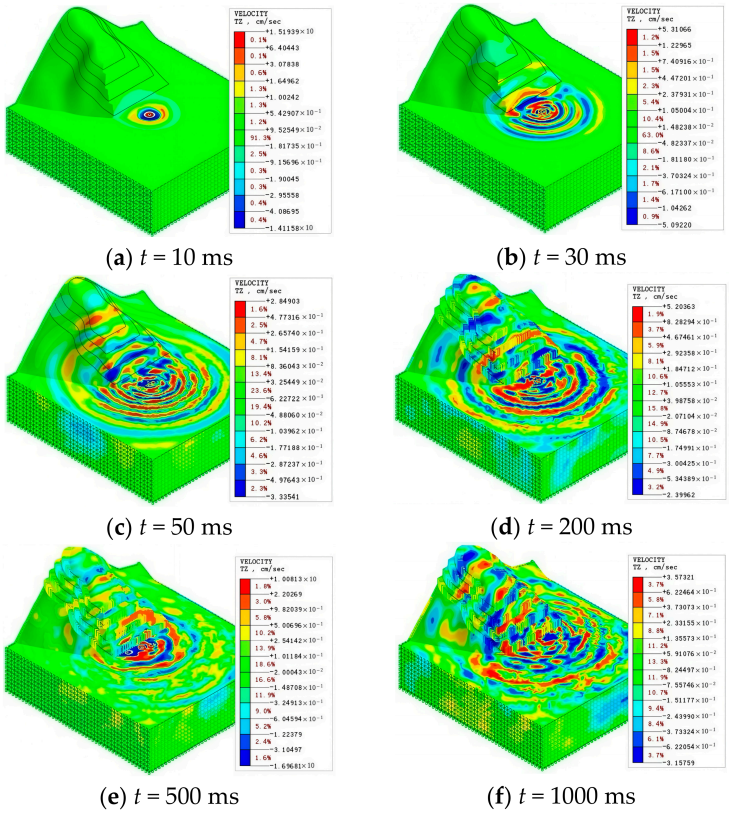


(**a**) t = 10 ms (**b**) t = 30 ms

(**c**) t = 50 ms (**d**) t = 200 ms

(**e**) t = 500 ms (**f**) t = 1000 ms

Figure 10. Vibration velocity contour of the rock mass in the Y-direction.



(**a**) t = 10 ms (**b**) t = 30 ms

(**c**) t = 50 ms (**d**) t = 200 ms

(**e**) t = 500 ms (**f**) t = 1000 ms

Figure 11. Vibration velocity contour of the rock mass in the Z-direction.

Furthermore, at any given temporal instant, an increase in both horizontal blast center distance and elevation does not necessarily correlate with a monotonic decrease in particle

vibration velocity. Instead, the velocity exhibits fluctuations during its overall attenuation, characterized by the emergence of several localized extreme vibration velocity points. Concurrently, an examination of the vibration velocity distribution on the slope surface reveals a tendency for the vibration velocity isolines to migrate towards the outer edge of the slope. In the proximity of the slope surface, the reflection of blast seismic waves by the free surface leads to a superposition effect, resulting in amplified vibrations. The outer edge of the bench, functioning as an additional structural component of the entire slope, experiences a more pronounced "whip-tail effect" under the influence of blasting.

3.5. Analysis of Dynamic Response Characteristics of Slope Surface Particles

To comprehensively investigate the vibration effects experienced by individual particles on the slope surface under explosive loading, a specific analysis line, as depicted in Figure 12, was delineated. This analysis line originates from the outer edge of the first bench situated above the blasting zone and extends progressively upwards along the slope surface, culminating at the outer edge of the slope crest.

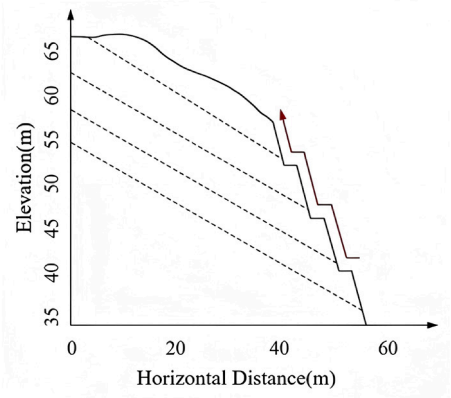


Figure 12. Surveying lines on slope. The dashed line represents a structural plane, and the arrow indicates the direction of the analysis line from the lower bench upward to the slope crest.

The peak particle velocity, maximum displacement, and stress values in various directions for each particle along the designated analysis line were meticulously extracted and subjected to detailed analysis. The resultant computational outcomes are graphically presented in Figure 13.

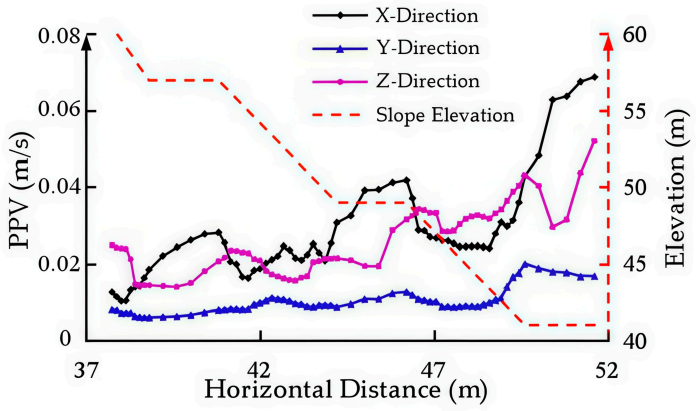


Figure 13. Peak particle velocity (ppv) of slope particles.

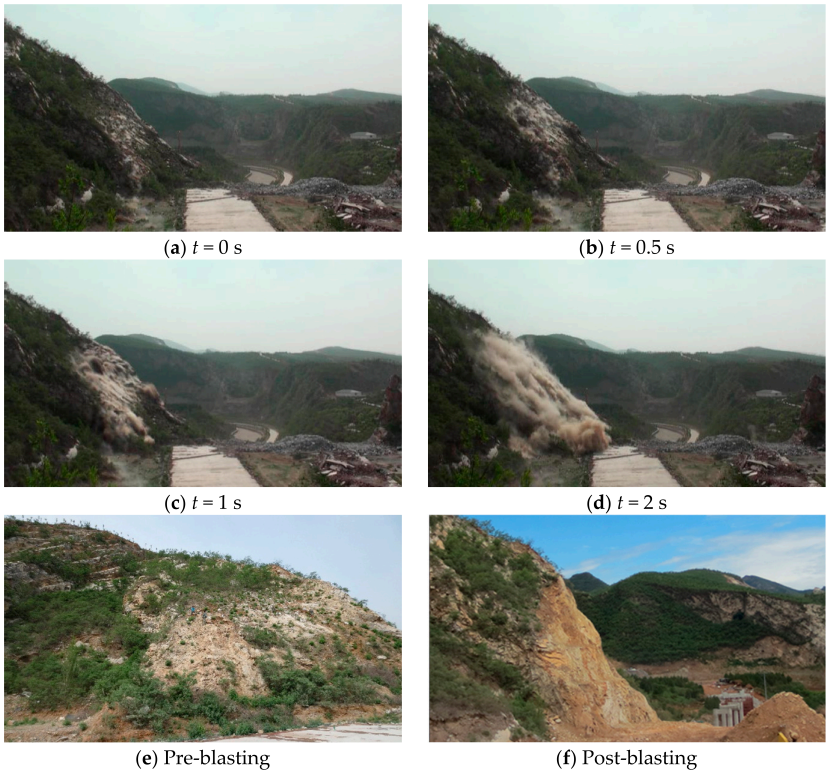
As elucidated by Figure 13, an upward progression along the slope surface corresponds to a gradual increase in both the horizontal blast center distance and the elevation difference relative to the blast source. This spatial variation leads to a rapid, albeit fluctuating,

attenuation of the blast vibration effect. Figure 13 distinctly illustrates the distribution patterns of both peak particle velocity and displacement. A critical examination of the curves reveals that the dynamic response of particles on the slope surface in the Y-direction is markedly less pronounced compared to the other two directions. In the immediate vicinity of the blast source, the dynamic response in the X-direction is marginally greater than that in the Z-direction; however, these two responses progressively converge during the attenuation phase. Based on the observed fluctuation patterns within the curves, it is evident that at the outer edge of the slope bench, the dynamic response of particles experiences a significant amplification attributed to the "whip-tail effect." This amplification phenomenon becomes more pronounced as the proximity to the blast source increases.

The whip-tail effect is attributed to stress wave reflection and superposition at the free surface of each bench. The outer edge behaves like the tip of a cantilever, where wave amplification is maximized due to geometric slenderness. This amplification gradually decreases with ascending elevation as the wave energy dissipates.

4. Analysis of Blasting Effect

Figure 14a–d provide a sequential visual representation of the slope rock mass blasting process at different time intervals, while Figure 14e,f offer a comparative illustration of the slope's morphology before and after the blasting operation. A thorough examination of Figure 14 confirms the absence of fly rock throughout the entire blasting process, and no evidence of collapse or structural damage to the slope rock mass was observed. Post-cleaning, the slope surface contours remained distinct and well-defined. These observations collectively indicate that the blasting parameters were judiciously designed, and the implementation of millisecond-delay blasting technology effectively achieved the desired blasting outcomes, including the intended loosening control, while concurrently safeguarding the stability of the slope rock mass and ensuring the structural integrity of surrounding edifices.



(**a**) t = 0 s (**b**) t = 0.5 s (**c**) t = 1 s (**d**) t = 2 s (**e**) Pre-blasting (**f**) Post-blasting

Figure 14. Photos of the blasting process.

The measured and simulated PPV values (0.05186 m/s) are significantly below the maximum allowable PPV of 0.1~0.15 m/s specified for slope stability in medium-hard rock by the Chinese standard GB 6722-2014, confirming that the blasting design ensured slope stability.

The sequential rock fragmentation process during bench blasting at various time points is vividly illustrated in Figure 14. The rock mass, under the synergistic influence of explosive energy and the inherent potential energy within the medium, undergoes a series of physical and mechanical transformations, manifesting as bulging, loosening, collapse, and sliding. On-site observations, facilitated by high-speed cameras, unequivocally demonstrated the absence of fly rock. Furthermore, the slope remained stable post-blasting, exhibiting uniform rock fragmentation that fully conformed to design specifications. Crucially, all fragmented rock masses were contained within the designated design boundaries.

5. Conclusions

Multiple blasts were monitored at this site; one representative event was selected for detailed analysis. While the quantitative results are site-specific, the observed attenuation patterns and whip-tail characteristics provide general insights for similar slope geometries. Based on a specific background engineering project, this study conducted comprehensive field vibration monitoring during the bench blasting excavation of a rock slope. A robust numerical calculation model was subsequently developed to simulate the dynamic response of the rock slope, enabling a systematic analysis of the peak particle velocity, stress fields, and displacement fields within the rock mass. The principal conclusions derived from this investigation are as follows:

(1) At the slope crest, the peak particle velocity of particles consistently exhibits attenuation with increasing distance from the blast center. Furthermore, the rate of this attenuation progressively diminishes as the blast center distance increases.

(2) On the slope surface, a distinct elevation amplification effect is observed to occur on adjacent benches.

(3) A significant “whip-tail effect” is prominently manifested at the outer edge of individual benches, with its intensity gradually decreasing with ascending elevation. Although limited by site constraints, the five points at 5 m intervals along the crest were sufficient to capture the primary attenuation trend and the first occurrence of the whip-tail effect. Future studies with denser arrays are recommended.

(4) Post-blasting, the slope rock mass maintains its stability, characterized by clear contours and uniform rock fragmentation. These findings provide a valuable reference for the design and execution of similar engineering projects.

Building upon this systematic monitoring and analytical framework, future research endeavors should prioritize a thorough examination of blast vibration effects, including a detailed analysis of their vibration velocity distribution characteristics. Concurrently, the development and implementation of effective measures to control blast seismic effects are crucial to ensure the long-term stability and safety of all levels of bench slopes, particularly in consideration of potential blast vibration amplification phenomena. The Mohr–Coulomb continuum model was adopted as a first-order engineering approximation suitable for the scale of this analysis. However, the actual rock mass contains joints and discontinuities; future studies using discontinuum methods (e.g., UDEC, 3DEC) are recommended for detailed stability assessment.

Author Contributions: Conceptualization, J.C. and Y.C.; methodology, J.C. and W.G.; software, S.W. and X.Z.; validation, J.C. and Y.C.; formal analysis, J.C.; investigation, X.Z.; resources, W.G.; data curation, J.C.; writing—original draft preparation, J.C.; writing—review and editing, Y.C.;

visualization, S.W.; supervision, X.Z. All authors have read and agreed to the published version of the manuscript.

Funding: This work is supported by the Shanghai Sci-tech Co-research Program (26HB2705600), and the Beijing Postdoctoral Research Foundation (2022-ZZ-100).

Institutional Review Board Statement: Not applicable.

Informed Consent Statement: Not applicable.

Data Availability Statement: The original contributions presented in the study are included in the article, further inquiries can be directed to the corresponding author.

Conflicts of Interest: The authors declare no conflict of interest.

References

1. Li, X.F.; Li, Q.; Li, H.B.; He, L.H.; Hu, Z.W.; Xie, K.R.; Xia, X. An improved constitutive model for predicting blast-induced damage zones and surrounding rock pressure. *Int. J. Rock Mech. Min.* **2026**, *202*, 106504. [CrossRef]
2. Hu, L.; Chang, W.F.; He, B.G.; Zhang, W.; Zhao, J.; Yao, Z.B.; Jiang, M.F.; Li, H.P.; Fu, L.J. Failure characteristics and development mechanism of time-delayed rockburst in a tunnel excavated via the drilling and blasting method: A case study. *Tunn. Undergr. Space Technol.* **2026**, *173*, 107576. [CrossRef]
3. Huang, L.Q.; Wang, Z.W.; Liu, K.; Liu, H.L.; Li, M.J.; Shen, H.M.; Li, X.B. Damage distribution characteristics and space optimizations of the large-diameter deep multi-holes blasting in thick ore bodies. *Tunn. Undergr. Space Technol.* **2025**, *156*, 106264. [CrossRef]
4. Ding, X.H.; Yang, Y.Q.; Zhou, W.; An, W.; Li, J.Y.; Ebelia, M. The law of blast stress wave propagation and fracture development in soft and hard composite rock. *Sci. Rep.* **2022**, *12*, 17120. [CrossRef] [PubMed]
5. Zhang, S.H.; Gao, W.X.; Ye, M.B.; Liu, J.C.; Liu, L.S.; Li, X.S.; Hu, Y. Dynamic response characteristics of a rock slope under blasting excavation. *Bull. Eng. Geol. Environ.* **2021**, *80*, 8453–8464. [CrossRef]
6. Roy, M.P.; Mishra, A.K.; Agrawal, H.; Singh, P.K. Blast vibration dependence on total explosives weight in open-pit blasting. *Arab. J. Geosci.* **2020**, *13*, 531. [CrossRef]
7. Zhang, W.L.; Sun, X.Y.; Yuan, W.; Zheng, H.Q. Stability Analysis and Critical Sliding Surface Determination of a Three-Dimensional Rock Slope: A Case Study of an Open-Pit Limestone Mine. *Int. J. Geomech.* **2026**, *26*, 05026002. [CrossRef]
8. Li, Z.; Zhou, J.G.; Wu, Y.B.; Li, H.; Li, Y.J.; Hu, Y.; Gao, W.X.; Liu, H.S. Experimental study on the influence of decoupling coefficient on rock blasting fragmentation and energy. *Eng. Fract. Mech.* **2025**, *315*, 110779. [CrossRef]
9. Zhang, X.; Liu, Z.G.; Chang, S.; Xue, Y.L.; Zhang, J.Y. Study on damage characteristics and fracture mechanisms of coal under high stress environment during blasting. *Eng. Fract. Mech.* **2025**, *314*, 110772. [CrossRef]
10. Yang, E.; Wang, Z.Q.; Xu, Q. Blasting Vibration Characteristics Calculation Formula considering Cylindrical Charge Delay Time. *Shock Vib.* **2022**, *2022*, 8988153. [CrossRef]
11. Song, Z.F.; Ke, M.; Liu, X.L. Identifying Delay Time of Detonator for a Millisecond Blasting. *Adv. Civ. Eng.* **2021**, *2021*, 5592696. [CrossRef]
12. Wang, P.; Ma, Y.J.; Zhu, Y.J.; Zhu, J. Experimental Study of Blast-Induced Vibration Characteristics Based on the Delay-Time Errors of Detonator. *Adv. Civ. Eng.* **2020**, *2020*, 8877409. [CrossRef]
13. Chen, S.H.; Wu, J.; Zhang, Z.H. Influence of millisecond time, charge length and detonation velocity on blasting vibration. *J. Cent. South Univ.* **2015**, *22*, 4787–4796. [CrossRef]
14. Wang, Y.; Yang, Y.; Zhang, X.; Fan, Z.Y.; Hu, F.Q.; He, J.Q.; Zhao, J.B. Study on the Influence of Delay Time on the Propagation Law of Adjacent Blast Hole Cracks. *Buildings* **2025**, *15*, 2030. [CrossRef]
15. Yang, J.H.; Cai, J.Y.; Yao, C.; Zhang, X.B.; Liu, L.S. Discussion on blasting vibration monitoring for rock damage control in rock slope excavation. *Earthq. Eng. Eng. Vib.* **2022**, *21*, 53–65. [CrossRef]
16. Shi, X.Z.; Qiu, X.Y.; Zhou, J.; Chen, X.; Fan, Y.Q.; Lu, E.W. Application of Hilbert-Huang transform based delay time identification in optimization of short millisecond blasting. *Trans. Nonferrous Metal. Soc.* **2016**, *26*, 1965–1974. [CrossRef]
17. Li, H.C.; Chen, D.X.; You, G.G.; Han, H.X.; Zhang, Q.P.; Shen, C.H.; Duan, T.H.; Jiang, X.Y.; Wang, P. Research on non-stationary blasting vibration prediction models and analysis of equal-interval delay for vibration reduction. *Bull. Eng. Geol. Environ.* **2025**, *85*, 46. [CrossRef]
18. Chen, Y.L.; Tang, X.L.; Xu, L.T.; Du, X.; Wang, S.R.; Fernández-Steeger, T.M.; Rafig, A. Comparative study of multiple statistical damage mechanics models for rock behaviors under high temperature. *Constr. Build. Mater.* **2024**, *447*, 138049. [CrossRef]
19. Zhang, X.Y.; Yan, P.; Lu, W.B.; Cheng, Y.F.; Sun, C.Y.; Zhu, J.; Guo, W.F.; Cheng, X.K. Frequency spectrum characteristics of blast-induced vibration with electronic detonators in ground blasting. *J. Build. Eng.* **2023**, *74*, 106892. [CrossRef]

20. Li, C.X.; Yang, R.S.; Wang, Y.B.; Kang, Y.Q.; Zhang, Y.T. Theory and numerical simulation of deep hole cut blasting based on dispersed charge and staged detonation. *Int. J. Rock Mech. Min.* **2023**, *169*, 105453. [CrossRef]
21. Ke, B.; Pan, R.H.; Zhang, J.; Wang, W.; Hu, Y.; Lei, G.; Chi, X.W.; Ren, G.F.; You, Y.H. Parameter Optimization and Fragmentation Prediction of Fan-Shaped Deep Hole Blasting in Sanxin Gold and Copper Mine. *Minerals* **2022**, *12*, 788. [CrossRef]
22. Bao, C.Y.; Jiang, N.; Yao, Y.K.; Zhou, C.B.; Yang, Y.M.; Zhang, Z. Blast-induced ground vibration propagation and prediction in a sandstone slope with soft mudstone interlayer. *Int. J. Prot. Struct.* **2026**, *17*, 812–833. [CrossRef]
23. Rasa, A.Y.; Budak, A. Soil-structure-trench interaction effects on vibration isolation of multi-story structures. *J. Braz. Soc. Mech. Sci.* **2026**, *48*, 186. [CrossRef]
24. *GB 6722-2014*; Safety Regulations for Blasting. Standards Press of China: Beijing, China, 2014.
25. Li, L.N.; Zhong, D.W.; Zhang, C. Determination of Blasting Vibration Parameters Using Particle Swarm Optimization. In *2013 International Conference on Information Science and Technology (ICIST)*; IEEE: New York, NY, USA, 2013; pp. 326–329.
26. Lu, W.B.; Yang, J.H.; Chen, M.; Zhou, C.B. An equivalent method for blasting vibration simulation. *Simul. Model. Pract. Theory* **2011**, *19*, 2050–2062. [CrossRef]
27. Tiwari, R.; Chakraborty, T.; Matsagar, V. Dynamic Analysis of a Twin Tunnel in Soil Subjected to Internal Blast Loading. *Indian Geotech. J.* **2016**, *56*, 369–380. [CrossRef]
28. Ozer, U. Environmental impacts of ground vibration induced by blasting at different rock units on the Kadikoy-Kartal metro tunnel. *Eng. Geol.* **2008**, *100*, 82–90. [CrossRef]

Disclaimer/Publisher's Note: The statements, opinions and data contained in all publications are solely those of the individual author(s) and contributor(s) and not of MDPI and/or the editor(s). MDPI and/or the editor(s) disclaim responsibility for any injury to people or property resulting from any ideas, methods, instructions or products referred to in the content.